APL Photonics ARTICLE pubs.aip.org/aip/app

Enhanced quantum correlations from joint pump and photon pair scattering

Cite as: APL Photon. 11, 066124 (2026); doi: 10.1063/5.0312389
Submitted: 16 November 2025 • Accepted: 1 June 2026 •
Published Online: 25 June 2026

Mamoon Safadi,[1,a] Nir Kuchuk,[1] Ohad Lib,[1] Yaron Bromberg,[1] and Arthur Goetschy[2]

AFFILIATIONS

[1] Racah Institute of Physics, The Hebrew University of Jerusalem, Jerusalem 91904, Israel
[2] ESPCI Paris, PSL University, CNRS, Institut Langevin, 1 rue Jussieu, F-75005 Paris, France

[a] Author to whom correspondence should be addressed: mamoon.safadi@mail.huji.ac.il

ABSTRACT

Scattering of non-classical light is enabling new ways to study and control photon transport. However, advances in this field often rely on simplifying assumptions regarding the quantum light's generation and its source. In this work, we relax some of these assumptions and probe the behavior of entangled photon pairs passing through a disordered layer after being generated by a randomly scattered pump via spontaneous parametric down-conversion. We experimentally demonstrate that when the photon pairs are generated immediately after the pump is scattered, they retain a sharp angular correlation peak even after propagating through a dynamic scattering medium. Beyond this proof-of-principle experiment, we present a comprehensive theoretical and numerical analysis showing that these correlations persist for arbitrary separations between the pair-generation region and the entrance to the disordered medium, with qualitatively distinct behavior depending on whether scattering occurs before or after pair generation. In particular, we analyze how the width and strength of the angular correlations depend on the distance between the generation region and the disordered layer. When the pairs are generated after the pump is scattered, the correlation width increases with distance, while the correlation strength remains approximately constant. In contrast, when the pairs are generated first and subsequently scattered, the correlation width initially broadens and then narrows, accompanied by a modification in correlation strength. These findings represent a crucial step toward understanding quantum light generation in complex media and potentially exploiting it for quantum technologies.

I. INTRODUCTION

Over the past few decades, scattering of non-classical light has emerged as a rich field of study offering insights and applications that extend well beyond the classical realm.[1] For example, researchers have shown that spatially entangled photon pairs traversing through a static disordered medium [Fig. 1(a)] exhibit speckles, coined two-photon speckle, in the angle-resolved two-photon correlations,[2–6] with entanglement surviving multiple scattering upon probing all output modes.[5,7] Typically, interference effects wash out upon ensemble averaging over realizations of the disorder;[8–11] yet, coherent features can still emerge. In transmission geometry, the two-photon correlation map has revealed an enhancement of the non-classical light that depends on the properties of the entangled state, such as its symmetry[12] and its correlation size.[13] In reflection geometry, we have recently observed the analog of coherent backscattering (CBS) of classical light[14–17] with entangled photon pairs.[18] This phenomenon, coined two-photon CBS (2p-CBS), manifests as a 2-to-1 enhancement after disorder averaging, with a width determined by the fundamental scattering properties of the sample, primarily its transport mean free path.

When the pump beam that drives the generation of entangled photon pairs in a nonlinear crystal is itself scattered, it opens a new perspective on how disorder and nonlinearity interplay in the generation process [Fig. 1(b)]. In particular, wavefront shaping of the pump beam has been shown to control the spatial correlations of entangled pairs and compensate for scattering, allowing for the optimization of the coincidence map using well-established classical tools.[19–22] Moreover, the spatial coherence of the pump not only governs the structure of the generated correlations, but also affects the overall entanglement dimensionality.[23] Despite these advances, no attention has been given to scenarios in which both the pump and

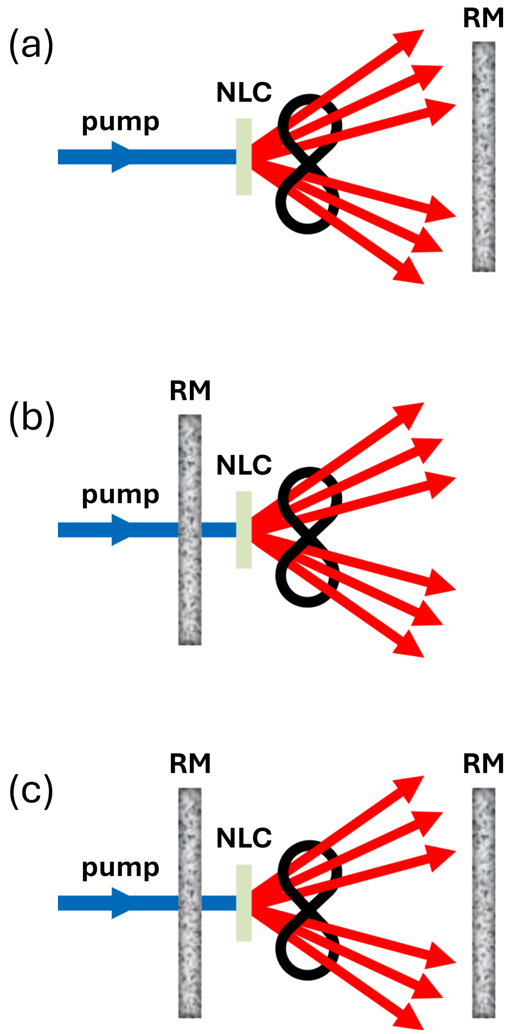

FIG. 1. (a) Post-generation scattering: The entangled photon pairs enter a random medium after being generated via spontaneous down-conversion (SPDC) from a typical plane-wave pump field. (b) Pre-generation scattering: The entangled pairs are generated from a scattered pump field. (c) Pre- and post-generation scattering: Both the pump field and the generated entangled pairs are scattered. NLC, nonlinear crystal; RM, random medium.

the entangled pairs undergo scattering [Fig. 1(c)], even though such conditions naturally arise when pairs are generated inside a nonlinear disordered medium. In contrast, the reversed classical process, second harmonic generation in random media, has been extensively studied both experimentally and theoretically.[24–37] Understanding the joint scattering of the pump and entangled pairs is, therefore, essential for uncovering the principles that enable coherent pair generation in complex environments.

In this work, we experimentally study the properties of entangled pairs when both the pump and the entangled pairs are scattered by a thin dynamic random medium, in the configuration where the pair-generation region and the random medium are in conjugate planes. We discover that despite the pump being scattered and scrambled, the down-converted photons, which also propagate through the same medium, retain enhanced correlations after disorder averaging when probing the coincidence counts. This effect bears a strong resemblance to the recently discovered 2p-CBS, despite the photons being generated within the scattering process. To explore the physical origin of this effect and its robustness beyond this proof-of-principle geometry, we conduct analytical modeling and numerical simulations, systematically varying the distance between the diffuser and the nonlinear crystal. Our results reveal that while the enhancement persists for both generation–scattering orderings, its evolution with distance depends on the ordering: when the pairs are generated after the pump is scattered, the correlation width increases, while the strength remains approximately constant, whereas when the pairs are generated first and then scattered, the width initially increases and then decreases, accompanied by a modification in correlation strength.

II. EXPERIMENT

Figure 2 depicts the experimental setup. A continuous-wave pump beam of waist $W_0 \approx 500$ μm and wavelength $\lambda = 405$ nm is imaged onto a rotating thin diffuser using lenses L_1 and L_2 of focal length 150 mm, and is subsequently imaged onto a nonlinear crystal using lenses L_3 and L_4 of focal length 100 mm. The diffuser chosen here is forwardly scattering and characterized by a scattering angle of $\theta_0 \approx 4.4$ mrad, as defined by the $\frac{1}{e}$ angular half-width of the far-field intensity distribution under plane-wave illumination. This choice of an anisotropic scattering medium allows for an efficient collection of photons using off-the-shelf low numerical aperture lenses, without compromising the underlying physics. Spatially entangled photon pairs of wavelength $\lambda = 810$ nm are then generated by spontaneous parametric down-conversion (SPDC), after which the pump beam is filtered out. The down-converted pairs propagate toward a mirror placed at a distance L from the crystal and are reflected back toward the diffuser. Notice that this configuration (diffuser–mirror) mimics a volumetric scatterer composed of two diffusers at a distance $2L$.[38–40] With the inclusion of the nonlinear crystal inside this fictitious volumetric diffuser, it mimics a simplified nonlinear disordered medium. The pairs then traverse lenses L_4, L_3, L_2, L_5 (focal

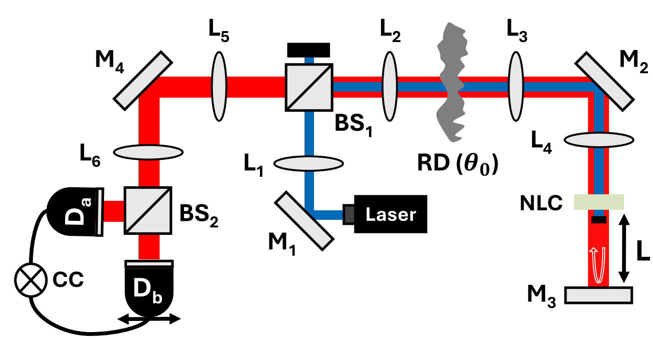

FIG. 2. Experimental setup. A pump beam passes through a rotating diffuser (RD), after which a nonlinear PPKTP crystal (NLC) generates entangled photon pairs via SPDC. The pairs propagate a distance L toward a mirror (M), reflect back, and scatter again from the rotating diffuser. Coincidence events are collected using two single-photon detectors: a static detector D_a and a scanning detector D_b, both positioned in the far-field of the diffuser. BS, beam splitter; θ_0, scattering angle; CC, coincidence circuit; L, lens.

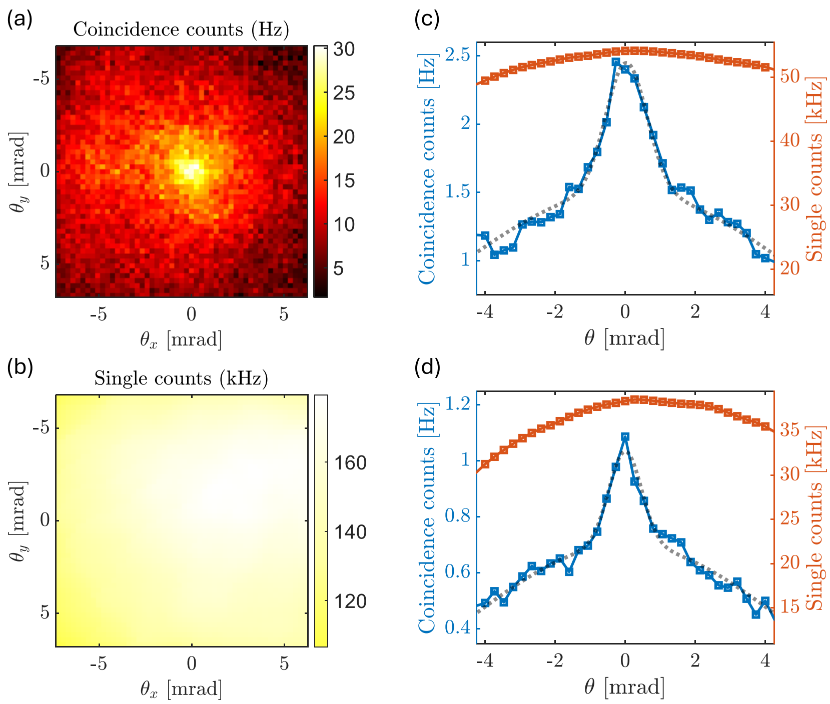

FIG. 3. (a) Measured two-dimensional coincidence map at the far-field of the random medium. The coincidence distribution exhibits a clear peak at $\theta = 0$. The transverse momenta are expressed in terms of angular positions such that $\theta_{x,y}$ denotes the transverse angular separation between the scanning (D_b) and static (D_a) detectors. Here, $L = 3.5$ cm. (b) The single counts registered by the scanning detector D_b exhibit a homogeneous angular distribution over the scanned region. Both the coincidence and single counts were acquired simultaneously using 100 μm core fiber-coupled detectors. (c) A one-dimensional scan of the peak for the same spacing L. Connected blue squares are the coincidence counts, with the connected orange squares being the single counts. To better resolve the peak, we used 50 μm core fibers. Here, the data were averaged over two independent scans around the peak. (d) An additional scan for a spacing of $L = 6$ cm. Once again, an enhanced cone is observed. The dotted lines in panels (c) and (d) indicate the fit according to the theory (see Sec. III A and Appendix A for more details on the fitting procedure).

length 150 mm), and L_6 (focal length 150 mm), placed in a 10-f configuration to image the far-field plane of the rotating diffuser. The far-field photon pair correlations are then measured at the back focal plane of L_6 using two single-photon detectors, one static (D_a) and the other scanned in the transverse dimension (D_b). A coincidence circuit (CC, Swabian Time Tagger 20) records the number of events in which two photons simultaneously arrive at the two detectors.

Figure 3(a) shows the two-dimensional coincidence map as a function of the transverse angular position of the scanning detector D_b (θ_b) relative to the static detector D_a (θ_a), measured at the far-field of the diffuser. Here and throughout this paper, the relative transverse angular separation is denoted by $\theta = \theta_b - \theta_a$. A clear enhanced area of the coincidences, around the origin, is observed, while the single counts distribution, shown in Fig. 3(b), reveals no discernible structure and appears nearly homogeneous. The absence of any feature in the single counts, when compared to the coincidence map, is a consequence of entanglement that is distributed across multiple spatial modes.[2,41] To better resolve the peak, we performed one-dimensional scans of the peak with a finer resolution [Fig. 3(c)]. To confirm our observations, the experiment was repeated at a different spacing, $L = 6$ cm [Fig. 3(d)]. Despite the change in spacing, a narrow enhanced cone is still observed, slightly narrower than in Fig. 3(c). Achieving a sufficient signal-to-noise ratio in the coincidence map required addressing two main noise sources: the speckle noise due to scattering and the Poisson noise due to the low flux of photon pairs reaching the detectors. To surpass the latter, we integrated each pixel in the coincidence map for tens of minutes to accumulate thousands of coincidence events per pixel. To surpass the speckle noise, the diffuser was rotated during the acquisition time, achieving a disorder averaged distribution.

III. THEORY

The above observation raises two questions: (1) Since the effect is characterized by a wide background with a narrow peak on top of it, as well as an almost 2-to-1 enhanced peak relative to the background, how is it related to CBS or its quantum counterpart, the 2p-CBS? (2) Is the observed effect unique to the case where the diffuser is imaged onto the crystal? In what follows, we turn to a theoretical analysis of both questions by studying the above effect as well as more general configurations. In particular, we consider scenarios in which the thin diffuser and thin crystal are not placed in conjugate planes. These general configurations go beyond the configuration realized in the present experiment (see Appendix A for a discussion of the experimental limitations that prevent their conclusive experimental test). To this end, we developed a model and performed numerical simulations to analyze the resulting spatial correlations. Notably, the diffuser–mirror configuration enables us to construct a comprehensive theoretical framework that captures the key processes governing the scattering of entangled photon pairs and the emergence of the enhanced correlation region.

The general two-photon state generated by SPDC can be described as $|\psi\rangle \propto \sum_{s,i} \Psi_{\mathbf{q}_s,\mathbf{q}_i} \hat{c}^\dagger_{\mathbf{q}_s} \hat{c}^\dagger_{\mathbf{q}_i} |0\rangle$, where $\hat{c}^\dagger_{\mathbf{q}_i}$ is the creation operator of an incident mode with transverse momentum $\mathbf{q}_i$, and $\Psi_{\mathbf{q}_s,\mathbf{q}_i}$, the two-photon amplitude, is determined by the pump beam and crystal parameters, and defines the input state.[42] In the special case of a thin crystal and a plane-wave pump with zero transverse momentum, the two-photon amplitude reduces to a delta function, $\Psi_{\mathbf{q}_s,\mathbf{q}_i} \propto \delta_{\mathbf{q}_s,-\mathbf{q}_i}$, yielding the well-known Einstein–Podolsky–Rosen (EPR) state.[42,43] More generally, however, it is determined by its angular spectrum,[42,44] which is the Fourier transform of the transverse pump field ψ_p, impinging on the thin crystal and evaluated at the sum coordinate, $\Psi_{\mathbf{q}_s,\mathbf{q}_i} = \mathscr{F}[\psi_P](\mathbf{q}_s + \mathbf{q}_i)$. The transverse spatial properties of entangled photon pairs are determined by the coincidence counts, which are, in turn, proportional to the two-photon correlation function $\Gamma_{ba} = \overline{\langle\psi| : \hat{n}_{\mathbf{q}_a}\hat{n}_{\mathbf{q}_b} : |\psi\rangle}$, where $\hat{n}_{\mathbf{q}} = \hat{d}^\dagger_{\mathbf{q}}\hat{d}_{\mathbf{q}}$ is the photon number operator of a mode with transverse momentum $\mathbf{q}$, $: (\ldots):$ stands for normal ordering, and $\overline{\ldots}$ represents ensemble averaging over different realizations of disorder.

For the subsequent analysis, it is useful to interpret the correlation function Γ_{ba} as the intensity of a two-photon wave function, $\Gamma_{ba} = |\Psi^{\text{out}}_{\mathbf{q}_b,\mathbf{q}_a}|^2$, where $\Psi^{\text{out}}_{\mathbf{q}_b,\mathbf{q}_a} = \langle 0|\hat{d}_{\mathbf{q}_a}\hat{d}_{\mathbf{q}_b}|\psi\rangle$. The operators for the outgoing and incoming modes, $\hat{d}_{\mathbf{q}}$ and $\hat{c}_{\mathbf{q}}$, are related through classical input–output relations, $\hat{d}_{\mathbf{q}_a} = \sum_{a'} G_{\mathbf{q}_a,\mathbf{q}_{a'}}\hat{c}_{\mathbf{q}_{a'}}$,[45] where the Green's matrix G describes linear propagation between the crystal and the detectors. We thus obtain the useful form $\Psi^{\text{out}}_{\mathbf{q}_b,\mathbf{q}_a} = [G\Psi G^T]_{\mathbf{q}_b,\mathbf{q}_a}$. In the following, we consider two scenarios where the crystal is placed either after or before the scattering layer and express in both cases the matrices Ψ and G in terms of transmission matrices representing free-space propagation over a distance s (modeled by a Fresnel kernel) and scattering by the thin diffuser, denoted $H^s(\omega)$ and $V(\omega)$, respectively. We explicitly write the dependence on the optical frequency ω to distinguish between the scattering and propagation of the photon pairs and those of the pump beam.

In the configuration considered in the experiment [Fig. 4(a)], the Green's matrix takes the form $G^+ = V(\omega)H^{d-z}(\omega)$, and the two-photon amplitude is given by $\Psi^+_{\mathbf{q},\mathbf{q}'} = [H^z(2\omega)V(2\omega)]_{\mathbf{q}+\mathbf{q}',\mathbf{0}}$, where $d = 2L$ and z is the axial position of the crystal relative to the diffuser. Here, the crystal is positioned after the diffuser $(z > 0)$, thereafter denoted as the positive z case. Substitution into the two-photon correlation function yields

$$\Gamma^+_{ba} \propto \overline{\left|\left\{\left[V(\omega)H^{d-z}(\omega)\right]\Psi^+\left[V(\omega)H^{d-z}(\omega)\right]^T\right\}_{\mathbf{q}_b,\mathbf{q}_a}\right|^2}. \quad (1)$$

By contrast, when the order of the crystal and the diffuser is reversed $(z < 0)$, a 2p-CBS configuration is obtained, with a propagation distance $|z|$ between the crystal and the scattering layer [Fig. 5(a)]. This case, hereafter, is denoted as the negative z case. The Green's matrix is then given by $G^- = V(\omega)H^d(\omega)V(\omega)H^{|z|}(\omega)$, while for a plane-wave pump, the two-photon amplitude is $\Psi^-_{\mathbf{q},\mathbf{q}'} \propto \delta_{\mathbf{q}+\mathbf{q}',\mathbf{0}}$. Substitution into the two-photon correlation function yields

$$\Gamma^-_{ba} \propto \overline{\left|\left\{\left[V(\omega)H^d(\omega)V(\omega)H^{|z|}(\omega)\right]\Psi^-\left[V(\omega)H^d(\omega)V(\omega)H^{|z|}(\omega)\right]^T\right\}_{\mathbf{q}_b,\mathbf{q}_a}\right|^2}. \quad (2)$$

To make further progress, we model the thin diffuser as a random complex screen with Gaussian statistics. In particular, we assume that the matrix $V(\omega)$ is diagonal in real space and that the field–field correlation function in real space is given by $\overline{V_{\rho,\rho}(\omega)V_{\rho',\rho'}(\omega)^*} = e^{-|\rho-\rho'|^2/4\xi_0^2}$, where ξ_0 sets the spatial correlation width of the field–field correlator, namely, the transverse coherence length. This corresponds to anisotropic scattering within an angular range $\theta_0 = 1/k\xi_0$, where $k = \omega/c$. In Appendix B, we discuss an alternative model of the diffuser, in which it is treated as a random phase screen with Gaussian phase statistics. Both models yield qualitatively consistent predictions for the two-photon correlation functions.

If we neglect material dispersion and amplitude fluctuations, we have $V_{\rho,\rho}(2\omega) \simeq V_{\rho,\rho}(\omega)^2$, since the phase imprinted by the screen is twice as large when the frequency doubles. As a result, the diffuser's behavior at frequency 2ω follows directly from its properties at ω via Gaussian contraction. In particular, $\overline{V_{\rho,\rho}(2\omega)V_{\rho',\rho'}(2\omega)^*} = 2\,\overline{V_{\rho,\rho}(\omega)V_{\rho',\rho'}(\omega)^*}^2$. In the transverse-momentum basis, the correlations of the matrix elements become

$$\begin{aligned}\overline{V_{\mathbf{q}_\alpha,\mathbf{q}_\beta}(\omega)V^*_{\mathbf{q}_\gamma,\mathbf{q}_\delta}(\omega)} &= F_\omega\left(\mathbf{q}_\alpha - \mathbf{q}_\beta\right)\delta_{\mathbf{q}_\beta-\mathbf{q}_\delta,\mathbf{q}_\alpha-\mathbf{q}_\gamma},\\ \overline{V_{\mathbf{q}_\alpha,\mathbf{q}_\beta}(2\omega)V^*_{\mathbf{q}_\gamma,\mathbf{q}_\delta}(2\omega)} &= F_{2\omega}\left(\mathbf{q}_\alpha - \mathbf{q}_\beta\right)\delta_{\mathbf{q}_\beta-\mathbf{q}_\delta,\mathbf{q}_\alpha-\mathbf{q}_\gamma},\end{aligned} \quad (3)$$

with $F_\omega(\mathbf{q}) \propto e^{-q^2\xi_0^2}$ and $F_{2\omega}(\mathbf{q}) \propto 2\sum_{\mathbf{q}_\alpha} F_\omega(\mathbf{q}-\mathbf{q}_\alpha)F_\omega(\mathbf{q}_\alpha)$.

Within this Gaussian model, both Γ^+_{ba} and Γ^-_{ba} contain products of four matrices $V(\omega)$ and four conjugates $V(\omega)^*$, whose ensemble average reduces, by the complex Gaussian moment theorem, to a sum over $4! = 24$ pairwise contractions. In what follows, we focus on the regime where, after propagating a distance d, the transverse spread of the beam diffracted by the diffuser, $d\theta_0$, exceeds the transverse coherence length ξ_0. Equivalently, for a given θ_0, the propagation distance d must exceed the longitudinal coherence depth $z_0 = \xi_0/\theta_0 = 1/k\theta_0^2$. In this limit, scattering contributions forcing light to revisit the same coherence area of the diffuser become negligible, leaving only four dominant pairwise contractions in Γ^+_{ba} and Γ^-_{ba}, respectively, as discussed in detail below.

A. Randomized pump—Γ^+

We first consider the positive-z configuration shown in Fig. 4(a). In this case, four dominant contractions contribute to Eq. (1). Since each contraction is doubly degenerate, they can be represented by the two diagrams shown in Fig. 4(b). In these diagrams, solid and dashed lines, respectively, denote the complex amplitude of the propagating field and its conjugate. Open circles (squares) represent scattering events for fields at frequency ω (2ω), and correlated pairs are connected by red lines. The weight of each diagram is obtained by assigning transverse momenta to the propagation lines, in accordance with the momentum conservation imposed by Eq. (3) (scattering events preserve the momentum difference between a field and its conjugate). Each propagation line carries a weight $H^z_\omega(\mathbf{q})$, corresponding to free-space propagation over a distance z with

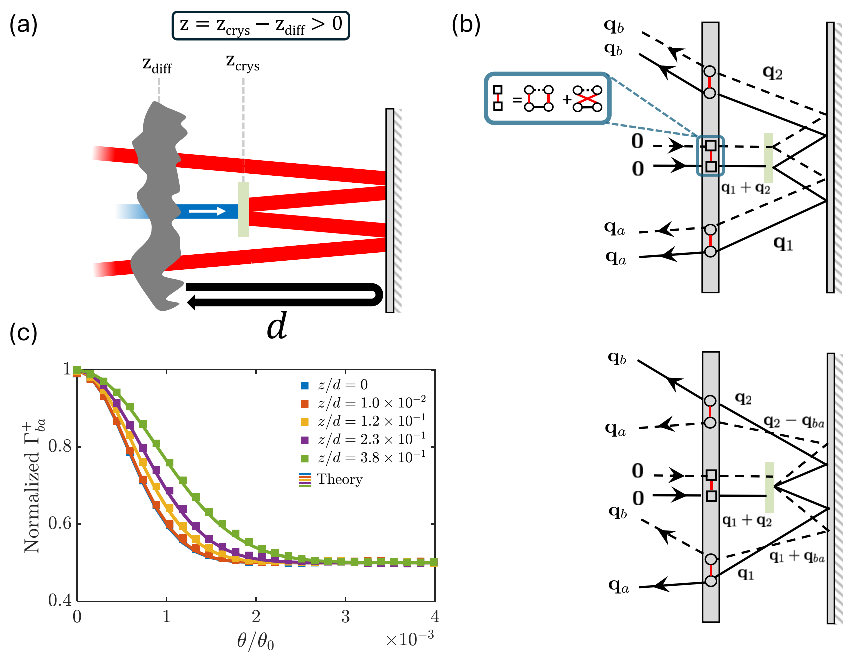

FIG. 4. (a) Simplified schematic of the experimental setup depicted in Fig. 2, with an additional pump-propagation distance z between the diffuser and the nonlinear crystal. (b) Diagrammatic representation of the four leading terms contributing to Γ^{+}_{ba}. Solid (dashed) lines represent the field (conjugate field). Open circles (squares) represent scattering events for the fields at frequency ω (2ω), while correlated pairs are denoted by a red line connecting them. Each propagating field line, or its conjugate, carries a weight $H^{z}_{\omega}(\mathbf{q})$ due to propagating a distance z at frequency ω, while each scattering vertex contributes $F_{\omega}(\Delta\mathbf{q})$ for a momentum transfer $\Delta\mathbf{q}$. The weight of each diagram is obtained by assigning transverse momenta to the propagation lines, in accordance with the momentum conservation imposed by the correlators. A summation is then performed over all free transverse momenta. The inset depicts the fact that the correlator at 2ω is a convolution of two correlators at ω. (c) Solid lines: plot of Eq. (5), the theoretical prediction for the two-photon correlation function in the $z > 0$ case, near the peak. Squares: the numerically obtained values for Γ^{+}_{ba} for the parameters used in the theory. The transverse angular separation is defined as $\theta = \theta_b - \theta_a$. Both the theoretical expression and the numerical data were first normalized to unit area and then by the peak value in the theoretical curve. Moreover, they are shown for $\theta_a = 0$. The numerics were realized in the limit where the angular spread exceeds the transverse coherence length, i.e., when $kd\theta_0^2 \gg 1$. See the text for more details.

transverse momentum $\mathbf{q}$ and frequency ω, while each scattering vertex contributes a factor $F_{\omega}(\Delta\mathbf{q})$ for a momentum transfer $\Delta\mathbf{q}$. A summation is then performed over all free transverse momenta. For instance, the total contribution of the two diagrams in Fig. 4(b) reads

$$\Gamma^{+}_{ba} \propto \sum_{\mathbf{q}_1,\mathbf{q}_2} F_{2\omega}(\mathbf{q}_2+\mathbf{q}_1)F_{\omega}(\mathbf{q}_b-\mathbf{q}_2)F_{\omega}(\mathbf{q}_a-\mathbf{q}_1) \times \Big[1 + H^{d-z}_{\omega}(\mathbf{q}_1)H^{d-z}_{\omega}(\mathbf{q}_1+\mathbf{q}_{ba})^{*}H^{d-z}_{\omega}(\mathbf{q}_2)H^{d-z}_{\omega}(\mathbf{q}_2-\mathbf{q}_{ba})^{*}\Big], \tag{4}$$

where $H^{z}_{\omega}(\mathbf{q}) = e^{iq^2 z/2k}$ is the Fresnel kernel associated with the matrix elements $H^{z}_{\mathbf{q},\mathbf{q}'}(\omega) = H^{z}_{\omega}(\mathbf{q})\,\delta_{\mathbf{q},\mathbf{q}'}$, and $\mathbf{q}_{ba} = \mathbf{q}_b - \mathbf{q}_a$. The degeneracy of each diagram is implicitly contained in the factor $F_{2\omega}(\mathbf{q}_2+\mathbf{q}_1)$, graphically represented in the inset of Fig. 4(b). We also note that the scattering of the pump photons does not introduce any dephasing during propagation between the diffuser and the crystal, since momentum conservation enforces the complex amplitude of the field and its conjugate to propagate in the same direction. Consequently, the dependence of Γ^{+}_{ba} on z arises solely from the dephasing of the photon pair as it propagates over the distance $d - z$ before being scattered by the diffuser into the directions $\mathbf{q}_a$ and $\mathbf{q}_b$.

Explicit calculation yields

$$\Gamma^{+}_{ba} \propto 2\,\exp\left[-\frac{(\boldsymbol{\theta}_a+\boldsymbol{\theta}_b)^2}{4\theta_0^2}\right]\left\{1+\exp\left[-\frac{(\boldsymbol{\theta}_a-\boldsymbol{\theta}_b)^2}{2\Delta\theta^{+}(z)^2}\right]\right\}, \tag{5}$$

where the detector positions are specified by their transverse angular positions, $\boldsymbol{\theta}_a = \mathbf{q}_a/k$ and $\boldsymbol{\theta}_b = \mathbf{q}_b/k$, and the angular width of the peak is given by

$$\Delta\theta^{+}(z) = \frac{1}{kd\theta_0(1 - z/d)}, \tag{6}$$

with $z \le d/2$. The envelope in Eq. (5) is centered at $\boldsymbol{\theta}_a + \boldsymbol{\theta}_b = 0$, since the photon pairs are created in opposite directions with respect to the scattered pump photons, and its width θ_0 reflects the angular range over which both the pump and the photon pairs are scattered. At the same time, a doubling of the coincidence count occurs for $\boldsymbol{\theta}_a - \boldsymbol{\theta}_b = 0$, showing that photons tend to emerge from the medium in the same direction, even though they were emitted in opposite directions.

This bunching effect is maintained within an angular range $\Delta\theta^{+}(z)$, inversely proportional to the transverse spatial extent $(d - z)\theta_0$ probed by the scattered photons. The scaling of this angular range is analogous to that found for the coherent backscattering

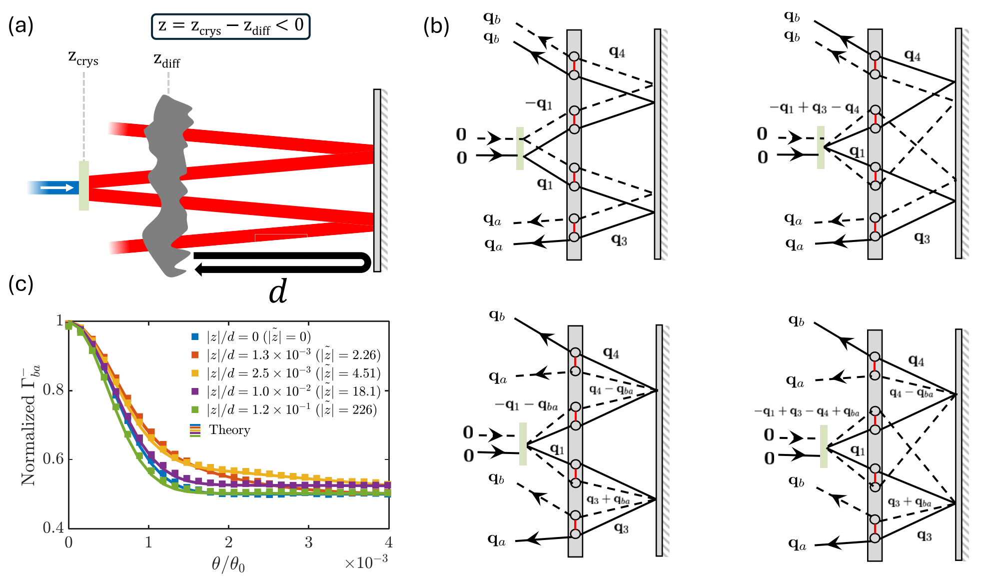

FIG. 5. (a) Simplified schematic of the 2p-CBS setup with an additional $|z|$ propagation toward the medium. (b) Diagrammatic representation of the four leading terms contributing to Γ^{-}_{ba}. The diagrammatic rules mentioned in the caption of Fig. 4 can be implemented here as well to arrive at a closed form for Γ^{-}_{ba}. (c) Solid lines: plot of Γ^{-}_{ba}, which is a summation of Eqs. (7) and (9). Squares: the numerically obtained values for Γ^{-}_{ba} for the parameters used in the theory. The normalization procedure and numerical parameters used here are identical to those mentioned in the caption of Fig. 4.

(CBS) effect, where the angular width is also determined by the inverse of the spatial region explored by the outgoing photons. More precisely and surprisingly, the result in Eq. (5) is identical to the correlation function obtained for the two-photon coherent backscattering (2p-CBS) configuration studied in Ref. 18, where the crystal is placed immediately before the scattering medium, provided that the distance d is replaced by $d - z$. This shows that positioning the crystal inside the disordered medium effectively reduces the transverse region probed by the photon pairs, thereby increasing the angular range over which they emerge in the same direction.

For the experimental results presented in Sec. II, the theoretical expression applies for $z = 0$ and for either choice of L. When fitting the experimental data [dashed lines in Figs. 3(c) and 3(d)], we observe a narrow enhanced region superimposed on a broader background. However, the measured width and enhancement do not exactly match the theoretical predictions. Our model assumes ideal angular resolution, i.e., point-like detection in the far-field, whereas the experimental setup has finite angular resolution, which effectively convolves the predicted line shape with the instrument response function. This convolution broadens the peak and reduces the observed enhancement relative to the theoretical values. A detailed description of the measurement process, fitting procedure, and limiting factors is provided in Appendix A.

To test the validity of Eq. (5), we ran numerical simulations for the two-photon correlation function, as modeled by Eq. (1). We numerically propagate each photon of the pair through a sequence of diffusers and free-space segments. Free-space propagation is realized by the standard Fresnel propagator. The diffusers are implemented by a complex transmission matrix, $V(\omega)$, generated in the Fourier domain by multiplying complex Gaussian random numbers by a Gaussian whose width corresponds to the scattering angle of the diffuser. The pump is modeled as a wide Gaussian beam, covering thousands of coherence areas of the diffuser, which propagates through the same diffuser at double the frequency, with scattering amplitude $V_{\boldsymbol{\rho},\boldsymbol{\rho}}(2\omega) = V_{\boldsymbol{\rho},\boldsymbol{\rho}}(\omega)^2$, and then through free space over a distance z. The simulation parameters were chosen to ensure that the angular spread per photon exceeds the transverse coherence length ξ_0. To this end, we selected $kd \approx 5697$ and $\theta_0 \approx 0.56$ rad such that $d/z_0 \gg 1$. Finally, to minimize the effect of speckle noise, the results were averaged over 10^5 random realizations of the diffuser. The results presented here correspond to 2D simulations (one transverse and one axial dimension); however, we have verified that identical behavior is obtained in 3D.

Figure 4(c) shows the simulated two-photon correlation Γ^{+}_{ba} for various distances z between the crystal and the diffuser, together with the corresponding theoretical prediction, obtained by the explicit calculation in Eq. (5) for $\boldsymbol{\theta}_a = 0$. For each distance, the numerical and theoretical curves were first normalized to unit area and then rescaled by a common factor such that the peak of the theoretical curve equals one. This two-step normalization eliminates arbitrary scaling and reduces noise sensitivity, isolating the line shape discrepancies. As our theory predicts, we indeed observe a doubling in the coincidences about the origin with a width that is monotonically increasing as z/d grows. The background, however, experiences no significant effect, further validating Eq. (5) (a much wider angular range is shown later in Fig. 7).

B. Plane-wave pump—Γ^{-}

Next, we study the negative-z configuration, where the crystal is positioned before the diffuser [Fig. 5(a)]. In contrast to the positive-z case, the four dominant contributions to Γ^{-}_{ba} in Eq. (1) are nondegenerate. They are represented by the four diagrams in Fig. 5(b), labeled according to the same transverse momentum conservation rules used in Fig. 4(b). This labeling reveals that the two diagrams in the left column (denoted $\Gamma^{-(1)}_{ba}$) behave differently from those in the right column (denoted $\Gamma^{-(2)}_{ba}$). In particular, for $\mathbf{q}_{ba} = \mathbf{0}$, the photon pairs contributing to $\Gamma^{-(1)}_{ba}$ do not experience any dephasing between the crystal and the diffuser, separated by a distance $|z|$, whereas such dephasing occurs in both contributions of $\Gamma^{-(2)}_{ba}$. This indicates that $\Gamma^{-(2)}_{ba}$ should vanish once $|z|$ exceeds the correlation depth z_0 of the diffuser. Conversely, when $z = 0$, the two diagrams in each row become indistinguishable (and thus degenerate), leading to the recovery of the 2p-CBS result reported in Ref. 18.

The expression of $\Gamma_{ba}^{-(1)}$ in terms of the correlation functions F_ω and propagation kernels H_ω^z can be obtained by applying the same diagrammatic rules as for Γ_{ba}^{+}. Here, we simply present the final result after explicitly evaluating the summation over all free transverse momenta,

$$\Gamma_{ba}^{-(1)} \propto \exp\left[-\frac{(\boldsymbol{\theta}_a+\boldsymbol{\theta}_b)^2}{4\theta_0^2}\right]\left\{1+\exp\left[-\frac{(\boldsymbol{\theta}_a-\boldsymbol{\theta}_b)^2}{2\Delta\theta_1^-(z)^2}\right]\right\}, \tag{7}$$

where we introduced the angular width

$$\Delta\theta_1^-(z) = \frac{1}{kd\theta_0\sqrt{1+2|z|/d+2(|z|/d)^2}}. \tag{8}$$

Similarly to Γ_{ba}^{+}, $\Gamma_{ba}^{-(1)}$ exhibits an envelope of width θ_0 and photon bunching at $\boldsymbol{\theta}_a = \boldsymbol{\theta}_b$, which is preserved within an angular range $\Delta\theta_1^-(z)$. Although in the negative-z configuration, the photon pair scatters twice from the diffuser, in the positive-z configuration, it scatters only once (see the corresponding diagrams), $\Delta\theta_1^-(z)$ and $\Delta\theta^+(z)$ exhibit the same linear dependence for $|z|/d \ll 1$. The difference thus appears only at higher orders in this parameter.

The evaluation of the two diagrams representing $\Gamma_{ba}^{-(2)}$ yields

$$\Gamma_{ba}^{-(2)} \propto \frac{\exp\left[-\frac{(\boldsymbol{\theta}_a+\boldsymbol{\theta}_b)^2+\tilde{z}^2(3\boldsymbol{\theta}_a^2+3\boldsymbol{\theta}_b^2-2\boldsymbol{\theta}_a.\boldsymbol{\theta}_b)}{4(1+\tilde{z}^2)\theta_0^2}\right]}{\sqrt{1+\tilde{z}^2}} \times\left\{1+\exp\left[-\frac{(\boldsymbol{\theta}_a-\boldsymbol{\theta}_b)^2}{2\Delta\theta_2^-(z)^2}\right]\right\}, \tag{9}$$

where $\tilde{z} = z/z_0$ denotes the position of the crystal in units of the correlation depth of the diffuser, and the angular width is

$$\Delta\theta_2^-(z) = \frac{\sqrt{1+\tilde{z}^2}}{kd\theta_0\sqrt{1+2|z|/d}}. \tag{10}$$

As anticipated, $\Gamma_{ba}^{-(2)}$ carries a global weight $\propto 1/\sqrt{1+\tilde{z}^2}$, which vanishes for $z \gg z_0$. In addition, unlike $\Delta\theta_1^-(z)$, the width $\Delta\theta_2^-(z)$ depends not only on z/d but also on z/z_0. In particular, for $|z| \lesssim z_0 \ll d$, $\Delta\theta_2^-(z)$ increases with $|z|$. This reflects the fact that, in the bottom-right diagram of Fig. 5(b), the entangled photons generated by the crystal are initially constrained to traverse the same coherence area of size ξ_0 within the diffuser. As a result, the effective transverse region probed by the outgoing photons is reduced, which broadens the angular range of photon bunching. Since $\Delta\theta_1^-(z)$ remains nearly constant for $|z| \lesssim z_0$, we thus expect the overall width of Γ_{ba}^- to increase in this regime due to the growth of $\Delta\theta_2^-(z)$. Conversely, for $|z| \gg z_0$, the contribution of $\Gamma_{ba}^{-(2)}$ becomes negligible, and the width of Γ_{ba}^- decreases following the behavior of $\Delta\theta_1^-(z)$.

Figure 5(c) shows the results of numerical simulations for the two-photon correlation Γ_{ba}^- [Eq. (2)], exhibiting the non-monotonic behavior discussed above. Apart from the reversal of scattering order and propagation paths, the normalization procedure and parameters are identical to those used for Γ_{ba}^+. Solid curves are the explicit calculation of $\Gamma_{ba}^- = \Gamma_{ba}^{-(1)} + \Gamma_{ba}^{-(2)}$ [sum of Eqs. (7) and (9)]. As expected, a sharp doubly enhanced peak is observed. The peak for $z = 0$ (blue) is identical to the peak of Γ_{ba}^+ in Fig. 4(c) (blue). Beyond $z = 0$, however, the width of Γ_{ba}^- broadens when $\tilde{z} \sim 1$ due to the contribution of $\Delta\theta_2^-(z)$ mentioned above, and tightens again for $|\tilde{z}| \gg 1$ due to $\Delta\theta_1^-(z)$ and the fact that the relative weight of $\Gamma_{ba}^{-(2)}$ decreases with $|\tilde{z}|$.

C. Comparison

To compare Γ_{ba}^+ and Γ_{ba}^-, we consider two figures of merit. First, Fig. 6(a) shows the full-width-at-half-maximum (FWHM) of the peak in the two-photon correlation function, $\Delta\theta$, normalized by the FWHM value at $z = 0$. The peak profile was obtained by subtracting the corresponding theoretical background from the simulation data (blue crosses). For reference, we also plot the theoretical width, derived in the same manner (orange solid line). As discussed above, while for $\tilde{z} > 0$, the width increases monotonically across the entire range, for $\tilde{z} < 0$, it exhibits a non-monotonic behavior, with a peak at $|\tilde{z}| \approx 2.1$.

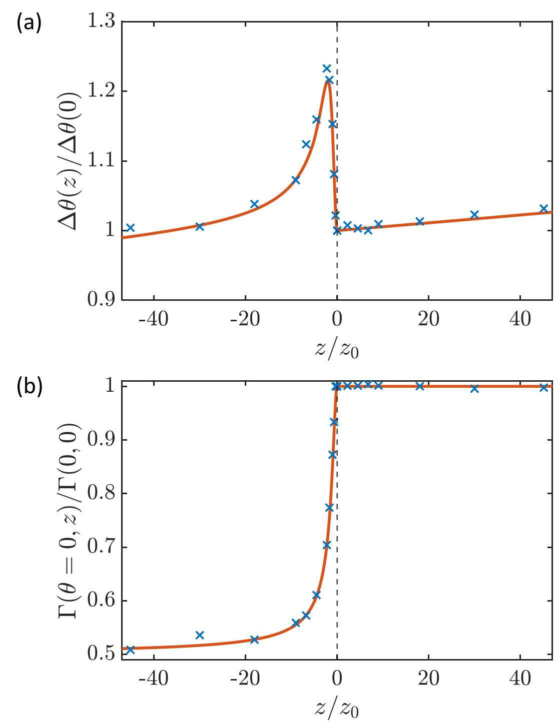

FIG. 6. (a) The width, $\Delta\theta$, defined as the full-width-at-half-maximum (FWHM) of the enhancement terms in $\Gamma_{ba}^{\pm}$, is extracted from numerical simulations (blue crosses) and compared to the theoretical prediction (orange line): for Γ_{ba}^+, the theory is given by Eq. (5), and for Γ_{ba}^-, the theory is given by the sum of Eqs. (7) and (9). To isolate the enhancement peak, we subtracted from the obtained two-photon correlation $\Gamma_{ba}^{\pm}$, the background terms in the aforementioned equations. . (b) Amplitude of $\Gamma_{ba}^{\pm}$ at $\theta = 0$. In both panels, the theory and numerical simulation values are normalized by their corresponding value at $z = 0$: the FWHM in panel (a) and the peak amplitude in panel (b).

Second, in Fig. 6(b), we show the peak coincidences normalized by the peak value of $\Gamma^{\pm}_{ba}$ at $z = 0$ (blue crosses). Once again, the theoretical amplitude is shown for reference (orange curve). As anticipated, the enhancement of Γ^{+}_{ba} is completely independent of $\tilde{z}$, while it experiences a sharp drop for increasing values of $|\tilde{z}|$ for Γ^{-}_{ba}, after which it plateaus at about 0.5. This can be easily understood from both contributions to Γ^{-}_{ba}, as the amplitude of $\Gamma^{-(2)}_{ba}$ vanishes for $|\tilde{z}| \gg 1$, while that of $\Gamma^{-(1)}_{ba}$ is constant, contributing half the total amplitude.

Within the Gaussian phase model considered in Appendix B, the behavior of $\Delta\theta$ shown in Fig. 6(a) is preserved (see Fig. 8 of Appendix B). The peak coincidence, however, shows a slight enhancement for $\tilde{z} < 0$, while maintaining a robust 2-to-1 ratio with respect to the background (see Fig. 9 of Appendix B).

Up to this point, we have primarily focused on the behavior of the peak of $\Gamma^{\pm}_{ba}$. For a complete characterization of the two-photon correlation functions, it is also important to assess the impact on the broad background. Figure 7 shows a much wider angular range than presented thus far, exhibiting the wide background of Γ^{+}_{ba} and Γ^{-}_{ba}. The insets display a zoomed-in portion of a background section (yellow shaded area), far from the peak. While the background of Γ^{+}_{ba} remains entirely unaltered for $z \neq 0$, in agreement with Eq. (5), Γ^{-}_{ba} undergoes a significant transition. In particular, the background tightens in the $|z| \lesssim z_0$ regime [blue to orange data in Fig. 7(b)], and as $|\tilde{z}|$ increases further (orange to green data), it relaxes back to the form observed at $z = 0$ (blue data), where the background width is set by θ_0. These features are consistent with the first terms of Eqs. (7) and (9), which predict that the envelope of $\Gamma^{-(1)}_{ba}$ has a constant width θ_0 independent of z, whereas the envelope of $\Gamma^{-(2)}_{ba}$ has a width $\sim\sqrt{(1+\tilde{z}^2)/(1+3\tilde{z}^2)}\,\theta_0$ and a weight $\sim 1/\sqrt{1+\tilde{z}^2}$. Qualitatively, similar features are obtained in the Gaussian phase model (see Fig. 9 of Appendix B).

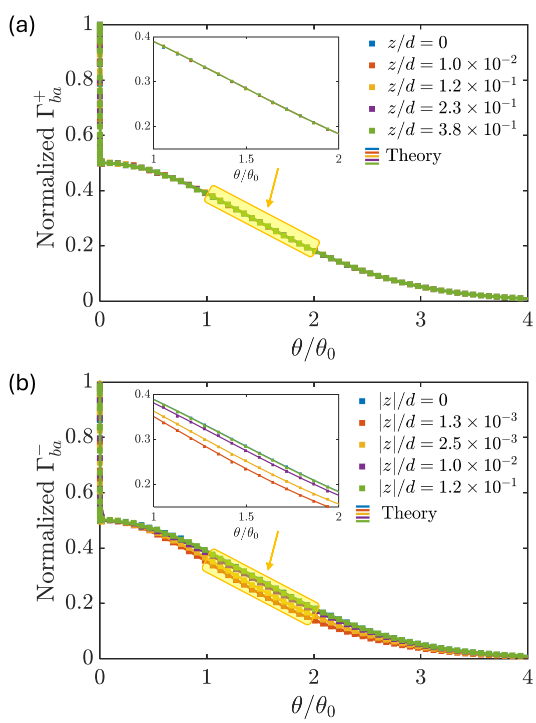

FIG. 7. Two-photon correlation Γ^{+}_{ba} (a) and Γ^{-}_{ba} (b), presented over a wider range than in Figs. 4 and 5. The insets show a magnified view of the shaded yellow region. For clarity, the marker density of the background was diluted to probe the behavior more clearly.

IV. CONCLUSIONS AND OUTLOOK

In conclusion, we experimentally and theoretically studied pair generation within a dynamically varying volumetric scatterer. We observed that, in this scenario, the pairs exhibit an enhancement of their two-photon correlations. We then generalized our findings to configurations where the diffuser and nonlinear crystal are placed at arbitrary positions relative to each other, covering cases such as pump scattering followed by pair generation and scattering, or unaltered pair generation followed by double scattering of the pairs. This generalization reveals the rich underlying physics of these processes, as supported by our numerical simulations. Even in this simplified engineered model of the medium, the observed correlations are sensitive to the sequence of scattering and pair generation, highlighting the complexity of their interplay inside a thick nonlinear scattering medium. We anticipate that this first step toward modeling photon-pair generation in the presence of multiple scattering, using a diagrammatic approach, will prove useful to uncover new phenomena and enable efficient pair generation within complex media.

ACKNOWLEDGMENTS

We acknowledge the insightful discussions with the late Chia Wei (Wade) Hsu. This research was supported by the Zuckerman STEM Leadership Program, the Israel Science Foundation (Grant No. 2497/21), and by the program "Investissements d'Avenir" launched by the French Government. M.S. acknowledges the support of the Israeli Council for Higher Education (VATAT).

AUTHOR DECLARATIONS

Conflict of Interest

The authors have no conflicts to disclose.

Author Contributions

Mamoon Safadi and Nir Kuchuk contributed equally to this work.

Mamoon Safadi: Formal analysis (equal); Investigation (equal); Methodology (equal); Software (equal); Writing – original draft (equal). **Nir Kuchuk**: Investigation (equal); Methodology (equal); Writing – review & editing (equal). **Ohad Lib**: Methodology (supporting); Writing – review & editing (supporting). **Yaron Bromberg**: Conceptualization (equal); Supervision (equal); Writing – original draft (equal). **Arthur Goetschy**: Conceptualization (equal); Supervision (equal); Writing – original draft (equal).

DATA AVAILABILITY

The data that support the findings of this study are available from the corresponding author upon reasonable request.

APPENDIX A: FITTING AND EXPERIMENTAL LIMITATIONS

Figures 3(c) and 3(d) display the experimental data for $L = 3.5$ cm and $L = 6$ cm, respectively, along with their fits to Eq. (5), in the model considered there. Each fit included fitting parameters accounting for the widths of each Gaussian (background and CBS) and the positions of the static and scanning detectors (which could introduce a relative skew between the background and the CBS peak). Although we observe that the enhancement width obtained for the larger spacing is, indeed, smaller than that of the shorter spacing, the experimental data turn out to be wider than the theoretical prediction, for both diffuser–mirror spacings L. For $L = 3.5$ cm, we predict an angular width of ~0.42 mrad, while the fit indicates a width of ~0.59 mrad. For $L = 6$ cm, our prediction states a width of 0.24 mrad, while the fit gives 0.46 mrad. We believe that these differences are due to the finite angular resolution of our experimental setup. To account for that, we convolve Eq. (5) with the mode profile of the detection apparatus, taken to be Gaussians of angular width σ/f, where σ is the radius of each collection fiber and f is the focal length of the far-field lens. Performing the convolution yields a peak of width $\Delta\theta^{+}(z=0) = \sqrt{(kd\theta_0)^{-2} + \delta_{2p,th}^2}$, where $\delta_{2p,th} = \sqrt{2}\sigma/f \approx 0.24$ mrad. While these adjusted peak widths improve the agreement with our predictions relative to the experimentally measured widths, they are still smaller by more than 20%. We attribute this to an angular resolution that is inferior to the theoretical prediction. To confirm this, we reverse engineered its value using the above equation and the experimental widths extracted. Doing so, we find that $\delta_{2p,\mathrm{exp}} \approx 0.4$ mrad for both measurements. This is likely due to the fact that the photon pairs are clipped by the aperture of the nonlinear crystal during the second pass through the crystal, thereby limiting their angular bandwidth.

APPENDIX B: GAUSSIAN PHASE MODEL

In the main text, we modeled the matrix elements of the diffuser's transmission matrix V as complex Gaussian random variables. This assumption allows higher-order moments of the scattered field to be reduced to pairwise contractions through the Gaussian moment theorem and makes the disorder averaging analytically tractable.

In this appendix, we consider a phase-only diffuser. In particular, the real-space transmission matrix elements are written as $V_{\boldsymbol{\rho},\boldsymbol{\rho}'}(\omega) = e^{ikD(\boldsymbol{\rho})}\delta_{\boldsymbol{\rho},\boldsymbol{\rho}'}$, where $D(\boldsymbol{\rho})$ denotes the diffuser thickness at transverse coordinate $\boldsymbol{\rho}$, and $k = \omega/c$. Hence, in the position-space representation at the diffuser plane, $V_{\boldsymbol{\rho},\boldsymbol{\rho}'}$ are not Gaussian random variables, since their amplitudes are unity. Rather, the Gaussian approximation becomes justified only after sufficient free-space propagation, through the mixing of transverse momentum components induced by the H^s propagators. Consequently, special care must be taken when considering propagation distances that are short relative to the diffuser's longitudinal coherence depth, z_0, where the Gaussian moment theorem does not apply.

Instead of assuming Gaussian statistics for V (*Gaussian field model*), we assume that the phase fluctuations induced by thickness variations of the medium are Gaussian (*Gaussian phase model*).[46] In particular, at position $\boldsymbol{\rho}$ and frequency ω, the fluctuating phase $\phi(\boldsymbol{\rho}) = kD(\boldsymbol{\rho})$ is taken to be a zero-mean real Gaussian random variable with correlator $\langle\phi(\rho)\phi(\rho')\rangle = k^2\sigma_D^2 \exp\left[-\Delta\rho^2/(2\ell^2)\right]$, where $\Delta\boldsymbol{\rho} = \boldsymbol{\rho} - \boldsymbol{\rho}'$, σ_D characterizes the amplitude of the thickness fluctuations, and ℓ is the correlation length of the diffuser. Under this assumption, the field–field correlation function $M(\Delta\boldsymbol{\rho}) \equiv \overline{V_{\boldsymbol{\rho},\boldsymbol{\rho}}(\omega)\, V^{*}_{\boldsymbol{\rho}',\boldsymbol{\rho}'}(\omega)}$ is given by $M(\Delta\boldsymbol{\rho}) = \exp\left\{-k^2\sigma_D^2\left[1 - \exp\left(-\frac{|\Delta\boldsymbol{\rho}|^2}{2\ell^2}\right)\right]\right\}$. In general, this spatial dependence is not Gaussian. However, in the limit of strong phase fluctuations, $k\sigma_D \gg 1$, the correlator is non-negligible only for small $\Delta\rho$. Expanding the inner exponential to leading order then gives $M(\Delta\boldsymbol{\rho}) \approx \exp\left(-\frac{|\Delta\boldsymbol{\rho}|^2}{4\xi_0^2}\right)$ with $\xi_0 = \ell/(\sqrt{2}k\sigma_D)$, which coincides with the Gaussian spatial field correlation function used in the main text. The corresponding momentum–space field–field correlation function is thus given by $\overline{V_{\mathbf{q}_\alpha,\mathbf{q}_\beta}(\omega)V^{*}_{\mathbf{q}_\gamma,\mathbf{q}_\delta}(\omega)} = F_\omega\left(\mathbf{q}_\alpha - \mathbf{q}_\beta\right)\delta_{\mathbf{q}_\beta-\mathbf{q}_\delta,\mathbf{q}_\alpha-\mathbf{q}_\gamma}$, where $F_\omega(\mathbf{q}) \propto \exp\left(-q^2\xi_0^2\right)$.

Importantly, although the correlator $M(\Delta\boldsymbol{\rho})$ becomes Gaussian in this limit, this does not imply that the matrix elements of V are themselves Gaussian random variables. Consequently, unlike in the Gaussian field model analyzed in the main text,

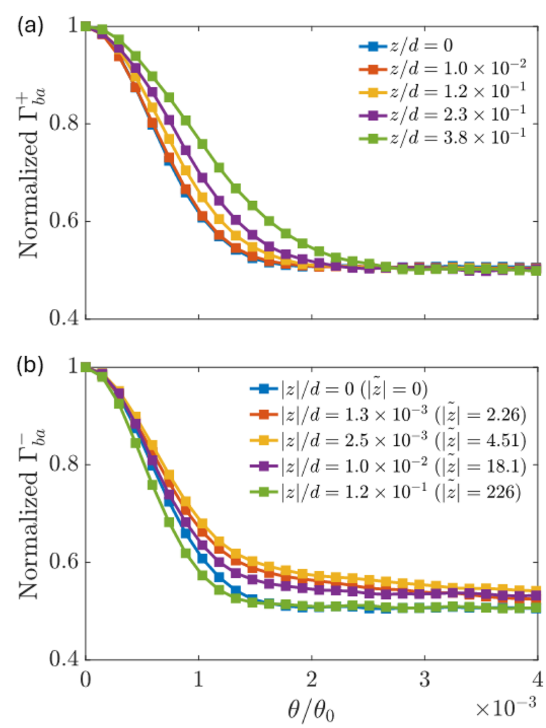

FIG. 8. Two-photon correlation functions in the Gaussian phase model considered here for different distances z. (a) Γ^{+}_{ba} shows the same monotonic increase in the peak width as in the Gaussian field model. (b) Γ^{-}_{ba} shows a similar non-monotonic behavior as the Gaussian field model, with the largest discrepancies appearing in the region $|\tilde{z}| \lesssim 10$.

the momentum–space correlations of $V(2\omega)$ cannot be obtained using the Gaussian moment theorem and must instead be computed directly. For a dispersionless diffuser, doubling the frequency doubles the phase imprinted by the screen so that the phase standard deviation increases by a factor of 2. Consequently, $\xi_0(2\omega) = \xi_0(\omega)/2$, and therefore, $F_{2\omega}(\mathbf{q}) \propto \exp\left[-q^2\xi_0^2(\omega)/4\right]$. Writing this in terms of angular variables $\boldsymbol{\theta} = \mathbf{q}/k$ and $\theta_0 = 1/k\xi_0 = \sqrt{2}\sigma_D/\ell$, we obtain $F_\omega(\boldsymbol{\theta}) \propto F_{2\omega}(\boldsymbol{\theta}) \propto \exp\left(-\theta^2/\theta_0^2\right)$. Thus, in the Gaussian phase model with strong phase fluctuations, the scattering angle is wavelength independent.

For the positive-z configuration, Γ_{ba}^+ involves products of two $V(\omega)$ matrices and one $V(2\omega)$ matrix, along with their three conjugate counterparts. Strictly speaking, the Gaussian moment theorem cannot be applied to evaluate the resulting six-field correlator via pairwise contractions. Nevertheless, since the scattering matrices V are evaluated at planes separated by a distance $d - z \gg z_0$, their matrix elements are well approximated by Gaussian random variables. Under this approximation, pairwise contractions yield the same equation as Eq. (4), with the only modification that $F_{2\omega}(\boldsymbol{\theta}) \propto \exp\left(-\theta^2/\theta_0^2\right)$, instead of $F_{2\omega}(\boldsymbol{\theta}) \propto \exp\left(-\theta^2/2\theta_0^2\right)$ as in the main text. Consequently, we obtain

$$\Gamma_{ba}^+ \propto \exp\left[-\frac{(\boldsymbol{\theta}_a + \boldsymbol{\theta}_b)^2}{6\theta_0^2}\right]\left\{1 + \exp\left[-\frac{(\boldsymbol{\theta}_a - \boldsymbol{\theta}_b)^2}{2\Delta\theta^+(z)^2}\right]\right\},$$

where the peak width is identical to that of the Gaussian field model [Eq. (6)], namely $\Delta\theta^+(z) = \left[kd\theta_0(1 - z/d)\right]^{-1}$. In other words, both the Gaussian phase model and the Gaussian field model yield the same enhanced peak in terms of amplitude, position, and width. The only difference is that the background is broadened from $2\theta_0$ to $\sqrt{6}\theta_0$.

To validate this approximation, we ran numerical simulations using the same parameters as in the main text, but with the Gaussian phase model considered here. In order to obtain the same scattering angle as in the Gaussian field model from the main text, we use $k\sigma_D \approx 4.3$ and $k\ell \approx 10.8$. The results correspond to 2D simulations, as in the main text. Figure 8(a) shows the simulated two-photon correlation function Γ_{ba}^+ for various distances z between the crystal and the diffuser, with each curve normalized to its peak value. The observed monotonic increase of the peak width of Γ_{ba}^+ is in excellent agreement with our prediction and the results of the Gaussian field model shown in Fig. 4(c).

Next, we study the negative-z configuration within the Gaussian phase model. In contrast to the positive-z case, however, a general analytical expression for Γ_{ba}^- is not readily obtainable. The reason is that Eq. (2) involves four matrices $V(\omega)$ and four conjugates $V(\omega)^*$, leading to an eight-field correlator that cannot, in general, be evaluated using the Gaussian moment theorem. Nevertheless, Γ_{ba}^- can be analyzed in two limiting regimes.

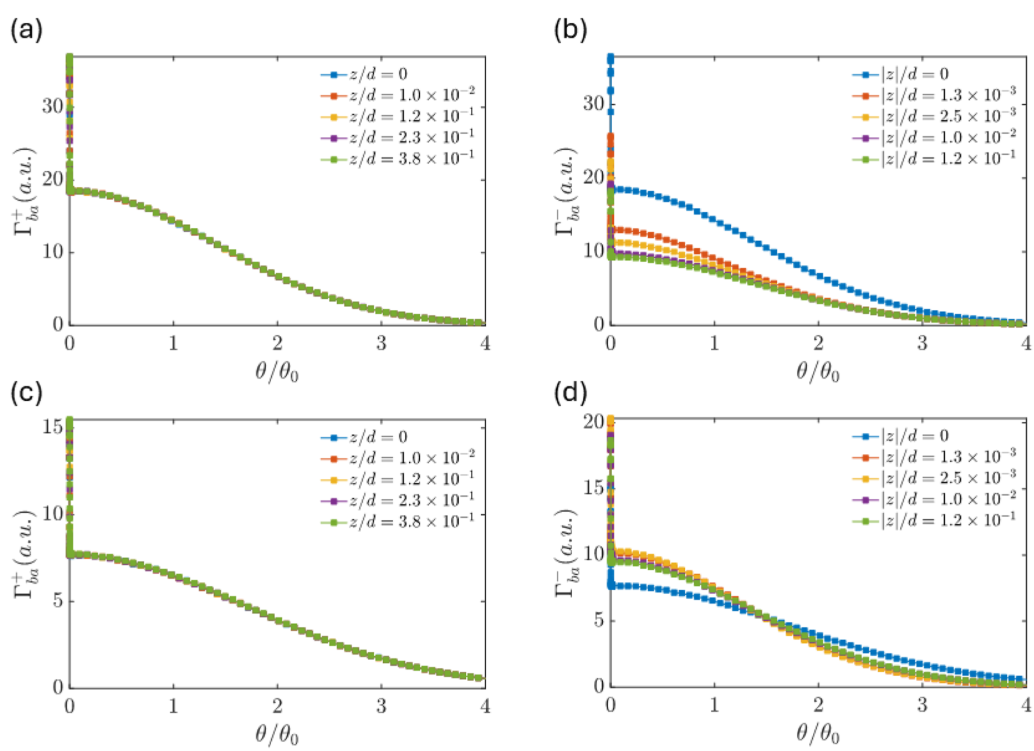

FIG. 9. Unnormalized two-photon correlation functions over a wider angular range, comparing the Gaussian field model used in the main text (top row) with the Gaussian phase model considered here (bottom row). Panels (a) and (c) show that although the background width of Γ_{ba}^+ differs between the two models, it remains essentially independent of z in both. In contrast, panels (b) and (d) show that the broad background of Γ_{ba}^- evolves with $|z|/d$, in a model-dependent way, while the two models asymptotically overlap for large values of $\tilde{z}$. In both models in all four panels, however, the peak-to-background ratio remains 2-to-1.

First, for $z, d \gg z_0$, the separation between the four planes at which the scattering matrices $V(\omega)$ are evaluated is much larger than the diffuser's longitudinal coherence depth, z_0. In this regime, the matrix elements of $V(\omega)$ can be approximated as complex Gaussian random variables, and the derivation of Eq. (7), therefore, remains valid also for the Gaussian phase model.

The second regime corresponds to $z = 0^-$ with $d \gg z_0$, where the propagation factor $H^{|z|}(\omega)$ reduces to the identity, and the two successive phase factors associated with the diffuser combine locally, with $V_{\rho,\rho}(\omega)^2 = V_{\rho,\rho}(2\omega)$. Thus, the scattering object in the $z = 0^-$ configuration is identical to that in the $z = 0^+$ configuration, yielding $\Gamma^-_{ba}(z = 0) = \Gamma^+_{ba}(z = 0)$.

We also perform numerical simulations to investigate the evolution of the two-photon correlation function Γ^- within the Gaussian phase model for several crystal–diffuser distances z. The results are shown in Fig. 8(b). Notably, the enhancement and its key features highlighted in the main text and in Fig. 5(c) for the Gaussian field model are also observed in the Gaussian phase model. The largest discrepancies appear in the region $|\tilde{z}| \lesssim 10$ [compare Figs. 5(c) and 8(b)].

Finally, we discuss the broad background and its characteristics. Figure 9 shows the unnormalized Γ^+_{ba} and Γ^-_{ba} over a much wider angular range, for both the Gaussian field model considered in the main text (top row) and the Gaussian phase model introduced in this appendix (bottom row). As expected, the background of Γ^+_{ba} remains entirely unaltered in both models [panels (a) and (c)], in agreement with our prediction. In contrast, the evolution of Γ^-_{ba} with $|z|$ differs between the two cases [panels (b) and (d)]. Within the Gaussian field model, the total coincidence rate decreases by a factor of 2 at large $|z|$, while the peak-to-background ratio remains fixed at 2-to-1. For the Gaussian phase model, however, the total coincidence rate is independent of $|z|$. Instead, the fraction of coincidences at the peak, relative to the total, decreases with $|z|$. At the same time, as the background broadens, the peak-to-background ratio remains robustly equal to 2-to-1, also in the Gaussian phase model.

REFERENCES

[1] O. Lib and Y. Bromberg, "Quantum light in complex media and its applications," Nat. Phys. **18**, 986–993 (2022).
[2] C. W. J. Beenakker, J. W. F. Venderbos, and M. P. van Exter, "Two-photon speckle as a probe of multi-dimensional entanglement," Phys. Rev. Lett. **102**, 193601 (2009).
[3] J. R. Ott, N. A. Mortensen, and P. Lodahl, "Quantum interference and entanglement induced by multiple scattering of light," Phys. Rev. Lett. **105**, 090501 (2010).
[4] M. Candé and S. E. Skipetrov, "Quantum versus classical effects in two-photon speckle patterns," Phys. Rev. A **87**, 013846 (2013).
[5] M. Candé, A. Goetschy, and S. E. Skipetrov, "Transmission of quantum entanglement through a random medium," Europhys. Lett. **107**, 54004 (2014).
[6] J. C. Schotland, A. Cazé, and T. B. Norris, "Scattering of entangled two-photon states," Opt. Lett. **41**, 444–447 (2016).
[7] N. H. Valencia, S. Goel, W. McCutcheon, H. Defienne, and M. Malik, "Unscrambling entanglement through a complex medium," Nat. Phys. **16**, 1112–1116 (2020).
[8] B.-J. Pors, C. H. Monken, E. R. Eliel, and J. P. Woerdman, "Transport of orbital-angular-momentum entanglement through a turbulent atmosphere," Opt. Express **19**, 6671–6683 (2011).
[9] A. Hamadou Ibrahim, F. S. Roux, M. McLaren, T. Konrad, and A. Forbes, "Orbital-angular-momentum entanglement in turbulence," Phys. Rev. A **88**, 012312 (2013).
[10] M. Krenn, J. Handsteiner, M. Fink, R. Fickler, and A. Zeilinger, "Twisted photon entanglement through turbulent air across Vienna," Proc. Natl. Acad. Sci. U.S.A. **112**, 14197–14201 (2015).
[11] N. D. Leonhard, V. N. Shatokhin, and A. Buchleitner, "Universal entanglement decay of photonic-orbital-angular-momentum qubit states in atmospheric turbulence," Phys. Rev. A **91**, 012345 (2015).
[12] M. P. van Exter, J. Woudenberg, H. Di Lorenzo Pires, and W. H. Peeters, "Bosonic, fermionic, and anyonic symmetry in two-photon random scattering," Phys. Rev. A **85**, 033823 (2012).
[13] O. Lib and Y. Bromberg, "Thermal biphotons," APL Photonics **7**, 031301 (2022).
[14] Y. Kuga and A. Ishimaru, "Retroreflectance from a dense distribution of spherical particles," J. Opt. Soc. Am. A **1**, 831–835 (1984).
[15] M. P. V. Albada and A. Lagendijk, "Observation of weak localization of light in a random medium," Phys. Rev. Lett. **55**, 2692 (1985).
[16] P.-E. Wolf and G. Maret, "Weak localization and coherent backscattering of photons in disordered media," Phys. Rev. Lett. **55**, 2696 (1985).
[17] E. Akkermans, P. E. Wolf, and R. Maynard, "Coherent backscattering of light by disordered media: Analysis of the peak line shape," Phys. Rev. Lett. **56**, 1471 (1986).
[18] M. Safadi, O. Lib, H.-C. Lin, C. W. Hsu, A. Goetschy, and Y. Bromberg, "Coherent backscattering of entangled photon pairs," Nat. Phys. **19**, 562–568 (2023).
[19] O. Lib, G. Hasson, and Y. Bromberg, "Real-time shaping of entangled photons by classical control and feedback," Sci. Adv. **6**, eabb6298 (2020).
[20] O. Lib and Y. Bromberg, "Pump-shaping of non-collinear and non-degenerate entangled photons," Opt. Lett. **45**, 6827–6830 (2020).
[21] R. Shekel, O. Lib, A. Sardas, and Y. Bromberg, "Shaping entangled photons through emulated turbulent atmosphere," OSA Continuum **4**, 2339–2350 (2021).
[22] P. Boucher, H. Defienne, and S. Gigan, "Engineering spatial correlations of entangled photon pairs by pump beam shaping," Opt. Lett. **46**, 4200–4203 (2021).
[23] H. Defienne and S. Gigan, "Spatially entangled photon-pair generation using a partial spatially coherent pump beam," Phys. Rev. A **99**, 053831 (2019).
[24] V. M. Agranovich and V. E. Kravtsov, "Effects of weak localization of photons in nonlinear optics: Second harmonic generation," Phys. Lett. A **131**, 378–386 (1988).
[25] E. V. Makeev and S. E. Skipetrov, "Second harmonic generation in suspensions of spherical particles," Opt. Commun. **224**, 139–147 (2003).
[26] R. Fischer, S. M. Saltiel, D. N. Neshev, W. Krolikowski, and Y. S. Kivshar, "Broadband femtosecond frequency doubling in random media," Appl. Phys. Lett. **89**, 191105 (2006).
[27] S. Faez, P. M. Johnson, D. A. Mazurenko, and A. Lagendijk, "Experimental observation of second-harmonic generation and diffusion inside random media," J. Opt. Soc. Am. B **26**, 235–243 (2009).
[28] C. Valencia and E. Méndez, "Weak localization effects in the second-harmonic light scattered by random systems of particles," Opt. Commun. **282**, 1706–1709 (2009).
[29] Y. Qiao, F. Ye, Y. Zheng, and X. Chen, "Cavity-enhanced second-harmonic generation in strongly scattering nonlinear media," Phys. Rev. A **99**, 043844 (2019).
[30] R. Savo, A. Morandi, J. S. Müller, F. Kaufmann, F. Timpu, M. Reig Escalé, M. Zanini, L. Isa, and R. Grange, "Broadband Mie driven random quasi-phase-matching," Nat. Photonics **14**, 740–747 (2020).
[31] J. S. Müller, A. Morandi, R. Grange, and R. Savo, "Modeling of random quasi-phase-matching in birefringent disordered media," Phys. Rev. Appl. **15**, 064070 (2021).
[32] A. Morandi, R. Savo, J. S. Müller, S. Reichen, and R. Grange, "Multiple scattering and random quasi-phase-matching in disordered assemblies of $LiNbO_3$ nanocubes," ACS Photonics **9**, 1882–1888 (2022).
[33] R. Samanta, R. Pierrat, R. Carminati, and S. Mujumdar, "Speckle decorrelation in fundamental and second-harmonic light scattered from nonlinear disorder," Phys. Rev. Appl. **18**, 054047 (2022).

[34] R. Samanta, R. Pierrat, R. Carminati, and S. Mujumdar, "Photon diffusion in space and time in a second-order-nonlinear disordered medium," Phys. Rev. A **108**, 053501 (2023).

[35] J. Moon, Y.-C. Cho, S. Kang, M. Jang, and W. Choi, "Measuring the scattering tensor of a disordered nonlinear medium," Nat. Phys. **19**, 1709–1718 (2023).

[36] R. Samanta, R. Savo, C. Conti, and S. Mujumdar, "Second-order nonlinear disordered photonic media," arXiv:2504.14589 (2025).

[37] A. Nardi, A. Morandi, R. Pierrat, A. Goetschy, X. Li, F. Scheffold, and R. Grange, "Mesoscopic light transport in nonlinear disordered media," Phys. Rev. Res. **7**, 023323 (2025).

[38] S. Schott, J. Bertolotti, J.-F. Léger, L. Bourdieu, and S. Gigan, "Characterization of the angular memory effect of scattered light in biological tissues," Opt. Express **23**, 13505–13516 (2015).

[39] X. Cheng, Y. Li, J. Mertz, S. Sakadžić, A. Devor, D. A. Boas, and L. Tian, "Development of a beam propagation method to simulate the point spread function degradation in scattering media," Opt. Lett. **44**, 4989–4992 (2019).

[40] P. Arjmand, O. Katz, S. Gigan, and M. Guillon, "Three-dimensional broadband light beam manipulation in forward scattering samples," Opt. Express **29**, 6563–6581 (2021).

[41] W. H. Peeters, J. J. D. Moerman, and M. P. van Exter, "Observation of two-photon speckle patterns," Phys. Rev. Lett. **104**, 173601 (2010).

[42] S. Walborn, C. Monken, S. Pádua, and P. Souto Ribeiro, "Spatial correlations in parametric down-conversion," Phys. Rep. **495**, 87–139 (2010).

[43] A. Einstein, B. Podolsky, and N. Rosen, "Can quantum-mechanical description of physical reality be considered complete?," Phys. Rev. **47**, 777 (1935).

[44] C. H. Monken, P. H. S. Ribeiro, and S. Pádua, "Transfer of angular spectrum and image formation in spontaneous parametric down-conversion," Phys. Rev. A **57**, 3123 (1998).

[45] C. W. J. Beenakker, "Random-matrix theory of quantum transport," Rev. Mod. Phys. **69**, 731–808 (1997).

[46] J. W. Goodman, *Speckle Phenomena in Optics: Theory and Applications* (Roberts and Company Publishers, 2007).